Science Advances

AAAS

advances.sciencemag.org/cgi/content/full/4/3/eaap9302/DC1

Supplementary Materials for

Mapping metabolic changes by noninvasive, multiparametric, high-resolution imaging using endogenous contrast

Zhiyi Liu, Dimitra Pouli, Carlo A. Alonzo, Antonio Varone, Sevasti Karaliota, Kyle P. Quinn, Karl Münger, Katia P. Karalis, Irene Georgakoudi

Published 7 March 2018, *Sci. Adv.* **4**, eaap9302 (2018)
DOI: 10.1126/sciadv.aap9302

The PDF file includes:

- Cell culture and treatment
- BAT preparation
- TPEF data acquisition
- Segmentation algorithm for BAT image analysis
- Calculation of heterogeneity index
- fig. S1. Schematic of integrated analysis processing.
- fig. S2. Raw data set for HFK cells under metabolic pathways of glycolysis or glutaminolysis, corresponding to representative images shown in Fig. 2.
- fig. S3. Raw data set for HL-1 cells under chemical uncoupling, corresponding to representative images shown in Fig. 3.
- fig. S4. Schematic of image segmentation of cytoplasm and lipids by taking into account both FAD fluorescence intensity and NADH bound fraction.
- fig. S5. Ex vivo and in vivo raw data set for BAT under the treatment of cold activation, corresponding to representative images shown in Fig. 4.
- fig. S6. Raw data set for C2C12 cells at various stages of β-oxidation, corresponding to representative images shown in Fig. 5 (A to F).
- fig. S7. Fluorescence images of C2C12 cells with MitoTracker Green FM staining under different fatty acids supplement.
- fig. S8. Raw data set for MSCs during lipogenesis, corresponding to representative images shown in Fig. 5 (G to L).
- fig. S9. Optical readouts of C2C12 myoblasts in response to hypoxia, glucose starvation, or CCCP-induced chemical uncoupling.
- fig. S10. Fluorescence images of C2C12 cells stained with tetramethylrhodamine ethylester (20 nM) under various treatments.

- fig. S11. Classification of metabolic pathways using only one or two of the three optical metrics.
- table S1. Individual heterogeneity index for each optical metric under different perturbation.
- Legends for movies S1 to S3
- List of abbreviations
- References (*98–100*)

Other Supplementary Material for this manuscript includes the following:
(available at advances.sciencemag.org/cgi/content/full/4/3/eaap9302/DC1)

- movie S1 (.avi format). Dynamic redox ratio maps of HFKs treated by normal media.
- movie S2 (.avi format). Dynamic redox ratio maps of HFKs treated by hypoxia media.
- movie S3 (.avi format). Dynamic redox ratio maps of HFKs treated by no-glucose media.

Supplementary Materials

Cell culture and treatment

Primary human foreskin keratinocytes (HFKs) were cultured and exposed to either control, hypoxia or glucose starvation conditions using protocols described in detail previously (*43*). HFKs were cultured on 50 mm glass bottom dishes (MatTek) until reaching confluence. Two types of media were prepared for different treatments: (i) media prepared in-house with the same glucose and glutamine concentrations as KSFM (Low Glu), or (ii) media prepared in-house with the same glutamine concentration as KSFM, but with no glucose (No Glu). Low Glu media were prepared by adding 1 g/L of glucose (Sigma-Alrich), and 584mg/L of L-glutamine (Sigma-Alrich) in no glucose, no glutamine, and no phenol red DMEM. No Glu media were prepared by adding 584mg/L of L-glutamine in no glucose, no glutamine, and no phenol red DMEM. Cells were exposed to Low Glu media for 1 hour before imaging. For the dynamic imaging (Fig. 2A-C), images were taken after exposure to Low Glu media (Normal media group), Low Glu media that had been nitrogen bubbled for 6 hour (Hypoxia group), or No Glu media (Glucose starvation group). Dynamic data were acquired from 3 dishes for each group. For the static imaging (Fig. 2D-I), images were taken immediately after exposure of HFKs to Low Glu media (Normal media group), immediately after exposure to Low Glu media that had been nitrogen bubbled for 6 hour (Hypoxia group), or after 30 min of exposure to No Glu media (Glucose starvation group). Static data were acquired from 4 dishes for each group, with a total of 16 fields per group (4 fields per dish).

Mouse HL-1 cardiomyocytes were maintained in Claycomb media (Sigma-Alrich) as described previously (*98*). Images were taken immediately after exposure to low-dose CCCP (50 μM) or vehicle. We prepared 4 dishes for each group, and acquired a total of 16 fields per group (4 fields per dish).

Mouse C2C12 myoblasts were maintained in DMEM supplemented with 10% fetal bovine serum. Cells were differentiated by replacing the medium with DMEM (glucose (+), pyruvate (+), glutamine (+)) containing 2% horse serum. After 3 days of differentiation, C2C12 cells expressing the muscle marker

desmin were starved for 4 hour, and then transferred to serum-free DMEM (SF-DMEM) containing 2% bovine serum albumin with or without fatty acids (Sigma-Alrich) (*99*). We treated cells with the unsaturated fatty acid oleate (200 μM) or the saturated fatty acid palmitate (200 μM). Vehicle-treated cells were used as controls. Data were acquired from 3 dishes for each group, with a total of 12 fields per group (4 fields per dish). SF-DMEM was also utilized for the hypoxia, glucose starvation and CCCP treatments. In the control group, cells were exposed to SF-DMEM for 1 hour before imaging. For the oxygen starvation and CCCP groups, cells were first exposed to SF-DMEM for 1 hour, and images were acquired immediately after exposure of C2C12 cells to 10 μM CCCP or to SF-DMEM that was nitrogen bubbled for 6 hours. For the glucose starvation group similarly, images were acquired after 1h exposure to SF-DMEM without glucose or pyruvate (glucose (-), pyruvate (-), glutamine (+)). Data were acquired from 4 dishes for each group, with a total of 20 fields per group (5 fields per dish).

Human mesenchymal stem cells (MSCs) were cultured using a previously established method (*29*). MSCs were isolated from bone marrow aspirate (Lonza, Walkersville, MD), and cultured in MSC proliferation medium consisting of minimum essential medium (MEM) α combined with 10% fetal bovine serum (FBS), 1% antibiotic/antimycotic, 1% non-essential amino acids (NEAA) and 1 ng/mL basic fibroblastic growth factor at 37°C with 5% CO2 in a humidified environment, until reaching confluence. Cell culture reagents were purchased from Life Technologies (Grand Island, NY) unless otherwise noted. To induce adipogenic differentiation, Dulbecco's Modified Eagle Medium with F12 nutrient mixture (DMEM/F12) was supplemented with 3% FBS, 1% antibiotic/antimycotic, human recombinant insulin (1 μM), dexamethasone (1 μM), pantothenate (17 μM), biotin (33 μM), 2,3-thiazolidinediones (5 μM), and 3-isobutyl-1-methylxanthine (500 μM). Induction factors were purchased from Sigma-Alrich. Data were acquired at 3 weeks post adipogenic differentiation induction. We prepared 4 dishes for each group, and acquired a total of 8 fields per group (2 fields per dish).

BAT preparation

All procedures involving animal tissues were approved by the Tufts University Institutional Animal Care and Use Committee (IACUC). Eight-week-old wild-type C57BL/6 male mice were housed in individual cages and acclimated at 18 °C for 2 days followed by cold exposure at 4 °C for another 2 days with a 12-hour light-dark cycle. Mice were given free access to standard laboratory chow and tap water. Acute cold exposure was applied based on previously established protocols well-tolerated by the animals for BAT formation and induction of UCP1 protein/gene expression levels (*100*). A control group of mice was housed at room temperature (22–25 °C) over the same period.

For *in vivo* imaging, BAT depots of mice (n = 3 mice per group) were surgically exposed, under isoflurane anesthesia. Briefly, after standard shaving and skin disinfection procedures, a lateral incision was made to expose the interscapular fat pads. Blunt forceps were then utilized to clamp the caudal edge of the interscapular fat pad and carefully retract cranially over the neck of the mouse, while preserving vascular and neural structures. A glass coverslip was then placed on top of the exposed depots and a minimal quantity of cyanoacrylate-latex glue was used to secure the animal's skin surrounding the exposed depots to the coverslip. Care was taken to protect the depots from glue exposure. The mouse was then flipped and secured on top of a stage of a custom built, inverted two-photon microscope. The entering branching artery into the BAT tissues was utilized as an anatomic guide for imaging (Fig. 4C). The positioning of the retracted depots cranially, along with the skin-coverslip adhesion and the weight of the mouse securing the tissue on the coverslip conjointly minimized motion artifacts related to breathing. Mouse body temperature was maintained with a custom heated stage. Imaging was initiated within 10 minutes of anesthesia induction and lasted maximally an additional 30 minutes. Anesthesia was induced using 3% isoflurane for 2-3 minutes and then maintained at 1.5%. Five fields were imaged per animal. If the image quality, which could be monitored on the screen, degraded during the 120 s integration time due to breathing motion, we stopped capturing the image and initiated a new acquisition to ensure good

contrast and resolution. After imaging, the mice were euthanized by isoflurane anesthesia followed by cervical dislocation.

For *ex vivo* BAT imaging, the animals (n = 3 mice per group) were directly euthanized by isoflurane anesthesia followed by cervical dislocation following the same cold treatment (cold exposure group) or room temperature acclimation (control group) as that for the in vivo study. Immediately upon sacrifice, interscapular fat depots were surgically exposed, BAT tissue isolated, snap frozen in dry ice and preserved at -80 °C until imaging. Six fields per mouse were imaged from the control and cold exposure groups respectively. For all BAT imaging, regions that exhibited strong second-harmonic generation were excluded from image acquisition to minimize extracellular matrix signal contributions.

TPEF data acquisition

For TPEF imaging, cell cultures were placed in home-made micro-incubator system, which maintained 37 °C and 5% CO_2 within a humidified environment throughout the imaging session. BAT tissue samples were placed on glass coverslips with PBS to prevent drying while imaging at room temperature, and the imaging was performed within 2 hours of tissue thawing. Images were obtained using a custom-built microscope with a 40 x water dipping objective (NA 1.1) or a 25 x water dipping objective (NA 0.95, for *in vivo* imaging only) equipped with a tunable (710-920 nm) Ti: sapphire laser (Mai Tai; Spectra Physics; Mountain View, CA). Emission events were registered by a photomultiplier tube (PMT) detector attached to a commercial time-correlated single photon counting (TCSPC) electronics module. To isolate NADH fluorescence, a 460(±20) nm emission filter (Chroma, ET460/40M-2P), corresponding to the NADH emission peak, was placed before the detector. NADH fluorescence images were acquired from this 460 nm detector using 755 nm excitation. FAD fluorescence was isolated using 525(±25) nm emission filter (Chroma, ET525/50M-2P) and 860 nm excitation. For cell cultures, images (512 x 512 pixels; 184 x 184 μm) were acquired with an integration time of 60 s, using a laser power of ~20 mW at 755 nm and ~15 mW at 860 nm. For *ex vivo* BAT tissue samples, images with the same resolution as for cell cultures were acquired with an integration time of 120 s, using a laser power of ~40 mW at 755 nm and ~30 mW at 860

nm. For *in vivo* BAT imaging, images (512 x 512 pixels; 294 x 294 μm) were acquired with an integration time of 120 s, using a laser power of ~99 mW at 755 nm and ~92 mW at 860 nm. Time-resolved fluorescence from a standard 7-hydroxycoumarin solution, which was assumed to have a constant fluorescence lifetime of 5.1 ns, was measured prior to each imaging session to monitor day-to-day consistency of instrumentation. We kept the gain of PMT constant throughout this study, and recorded the laser power of both 755 nm and 860 nm excitations for each experiment to normalize fluorescence intensity.

Segmentation algorithm for BAT image analysis

Different from cell images, BAT images have co-localized lipid and cytoplasm compartments, and algorithm was developed to separate cytoplasm from lipids, as shown in fig. S4. Firstly, three-level Otsu intensity thresholding was applied to both NADH and FAD images of each field (*97*), and two thresholds, referred to as the high or low Otsu threshold, divide the intensity to three levels. The lowest level was designated as low intensity background noise or weakly fluorescent cell compartments (e.g., nuclei), and regions assigned to the upper two quantized levels in corresponding NADH and FAD images were combined to define the complete cell or tissue area. These cell regions were further segmented into cytoplasm and lipid droplet compartments by combining FAD fluorescent intensity and bound NADH fraction information. Specifically, a lipid probability score was calculated for each pixel according to

$$P_{lipid} = \frac{2}{3}[1 - \min(\frac{I_{FAD}}{threshold_{FAD}}, 1)] + \frac{1}{3} f_{NADH}$$

where I_{FAD} is FAD fluorescence intensity, $threshold_{FAD}$ is the low Otsu threshold for FAD image, and f_{NADH} is the bound NADH fraction. If $P_{lipid} > 0.5$, then the pixel is classified as lipid, otherwise it is labeled as cytoplasm.

Calculation of heterogeneity index

The heterogeneity index of each optical biomarker was calculated using a previously established method (*96*). Briefly, based on the single cell data, frequency histograms were plotted for the optical redox ratio, NADH bound fraction and mitochondrial clustering. We fit the histograms to one-, two-, or three-component Gaussian curves, with the lowest Akaike Information Criterion indicating optimal fitting. The heterogeneity index is defined as $H = -\sum d_i p_i \ln p_i$, where i represents each Gaussian component, d represents the distance between the median of the Gaussian component and the median of all data within a biological replicate of a certain group, and p represents the proportion of this component (*96*). The heterogeneity indices of optical biomarkers in these experiments are shown in table S1, with the significance symbol revealing significant difference compared with corresponding control.

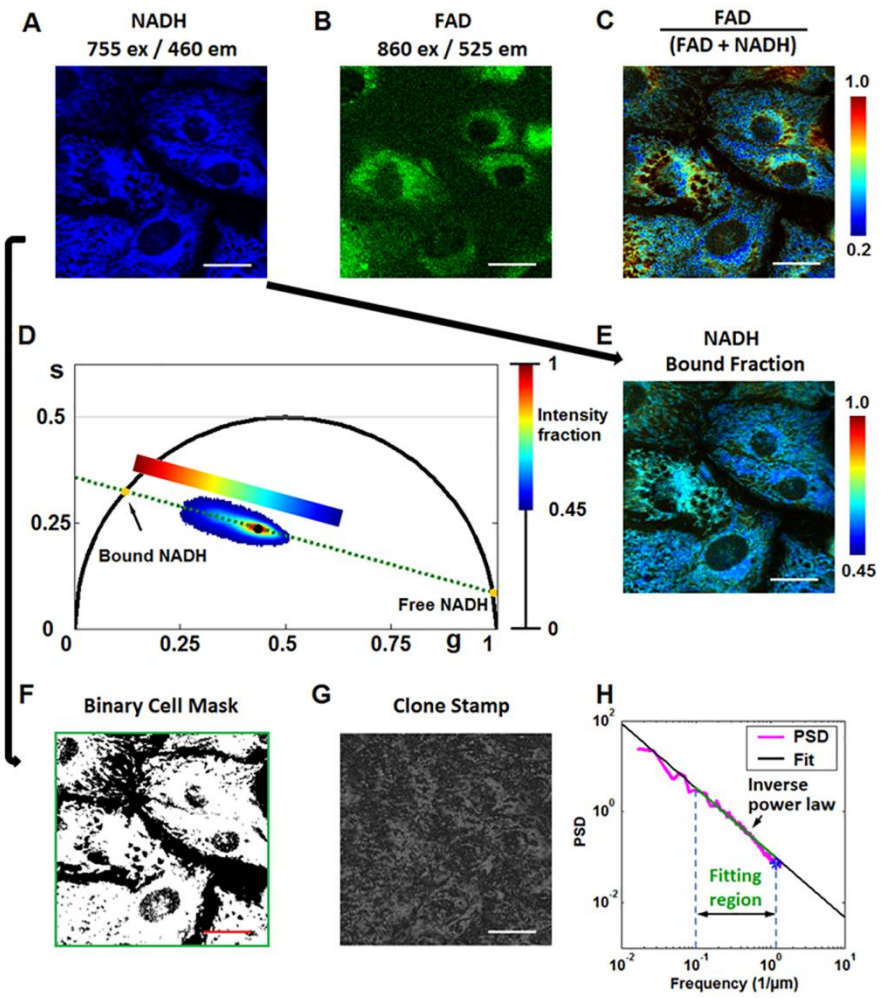

fig. S1. Schematic of integrated analysis processing. (**A**) Raw NADH image. (**B**) Raw FAD image. (**C**) Redox ratio map acquired from NADH and FAD images. (**D**) Phasor plot showing the clustering of pixels of an NADH image, according to the time decay at each pixel. A phasor is a graphical representation of the fluorescence intensity decay curve. The x and y axis represent the real (g) and imaginary (s) parts of the Fourier transform of the decay curve. The phasor of a mono-exponential decay is represented by a point on the universal semi-circle, with 0 and infinite lifetimes represented by the points with (1,0) and (0,0) coordinates respectively. For a bi-exponential decay, a phasor is represented by a point within the semi-circle. The phasors depicting the decay rates of many pixels within a field typically form an ellipse, whose major axis traverses the circle at the two points that represent the free (short) and bound (long) NADH lifetimes; its centroid provides an estimate of the intensity fraction of NADH found in bound form. (**E**) NADH bound fraction map acquired from the phasor analysis. (**F**) Binary mask of NADH image selecting the cytoplasm region of cells. (**G**) Clone stamped image of the NADH intensity signals within binary mask shown in (F). (**H**) PSD curve of the clone stamped image along with fitting curve. Scale bar: 30 μm.

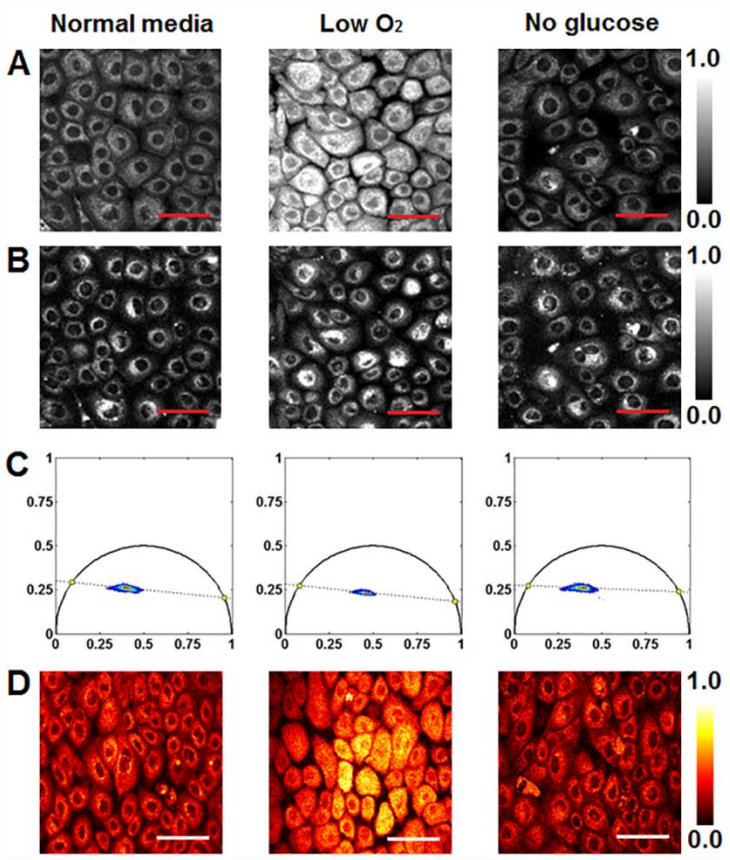

fig. S2. Raw data set for HFK cells under metabolic pathways of glycolysis or glutaminolysis, corresponding to representative images shown in Fig. 2. (**A**) Raw NADH and (**B**) raw FAD images used to generate redox ratio map. (**C**) Phasor plots showing the clustering of pixels in the g-s plane. (**D**) Raw NADH images corresponding to the clone stamped mitochondria images shown in Fig. 2H. Scale bar: 50 µm.

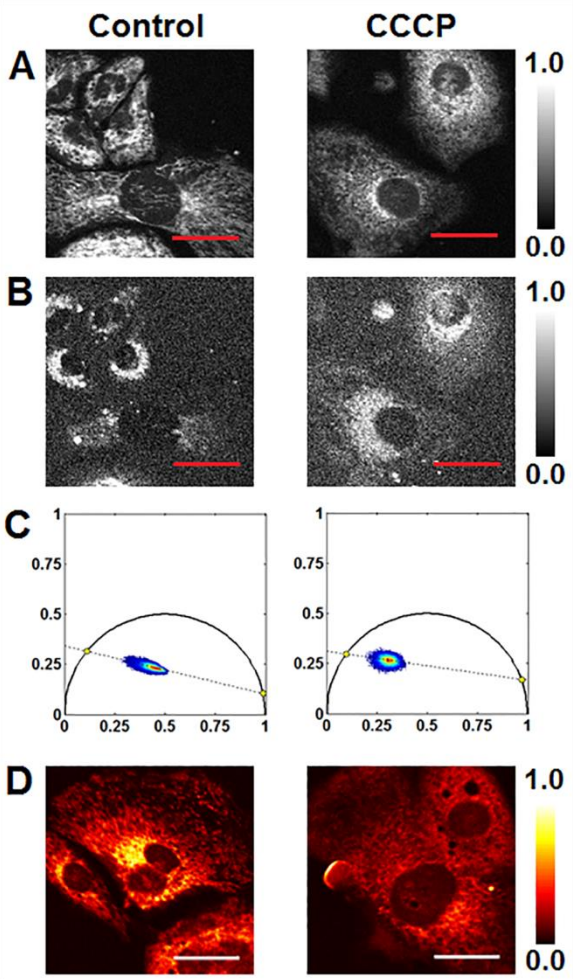

fig. S3. Raw data set for HL-1 cells under chemical uncoupling, corresponding to representative images shown in Fig. 3. (**A**) Raw NADH and (**B**) raw FAD images used to generate redox ratio map. (**C**) Phasor plots showing the clustering of pixels in the g-s plane. (**D**) Raw NADH images corresponding to the clone stamped mitochondria images shown in Fig. 3E. Scale bar: 30 µm.

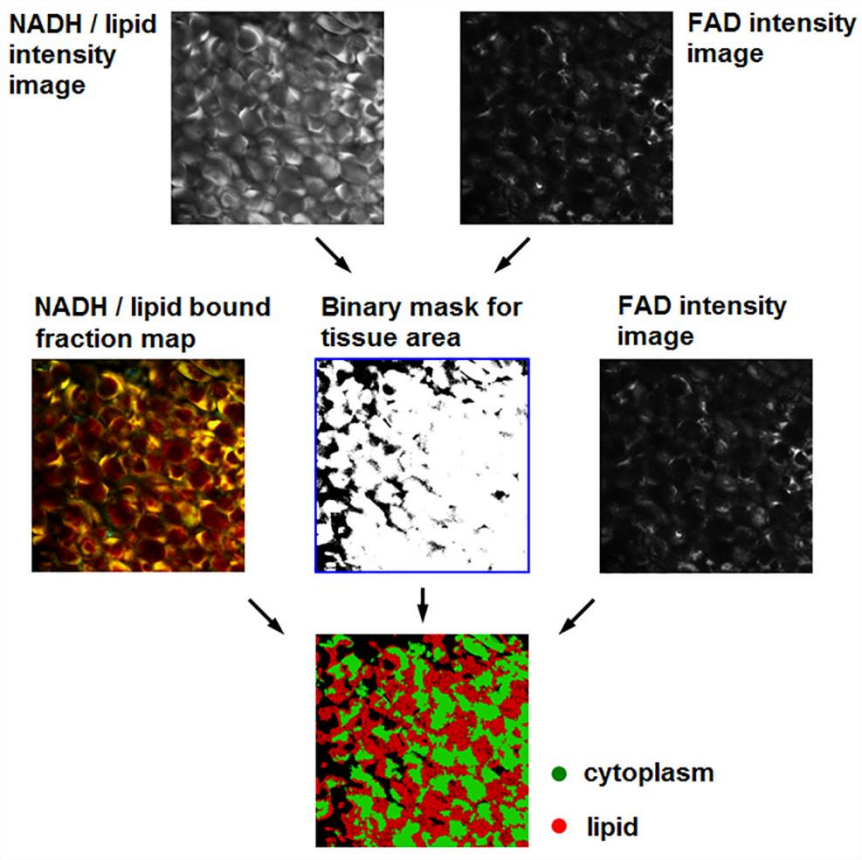

fig. S4. Schematic of image segmentation of cytoplasm and lipids by taking into account both FAD fluorescence intensity and NADH bound fraction. Firstly, low intensity regions are excluded which mainly correspond to background or nuclei which are weakly fluorescent. Based on cell morphology, lipids exhibit low fluorescence intensity in the FAD channel and high protein bound fraction in the NADH channel. These two criteria are weighted in assigning each pixel in an image either a cytoplasm or lipid label. See Supplementary Methods for more detail.

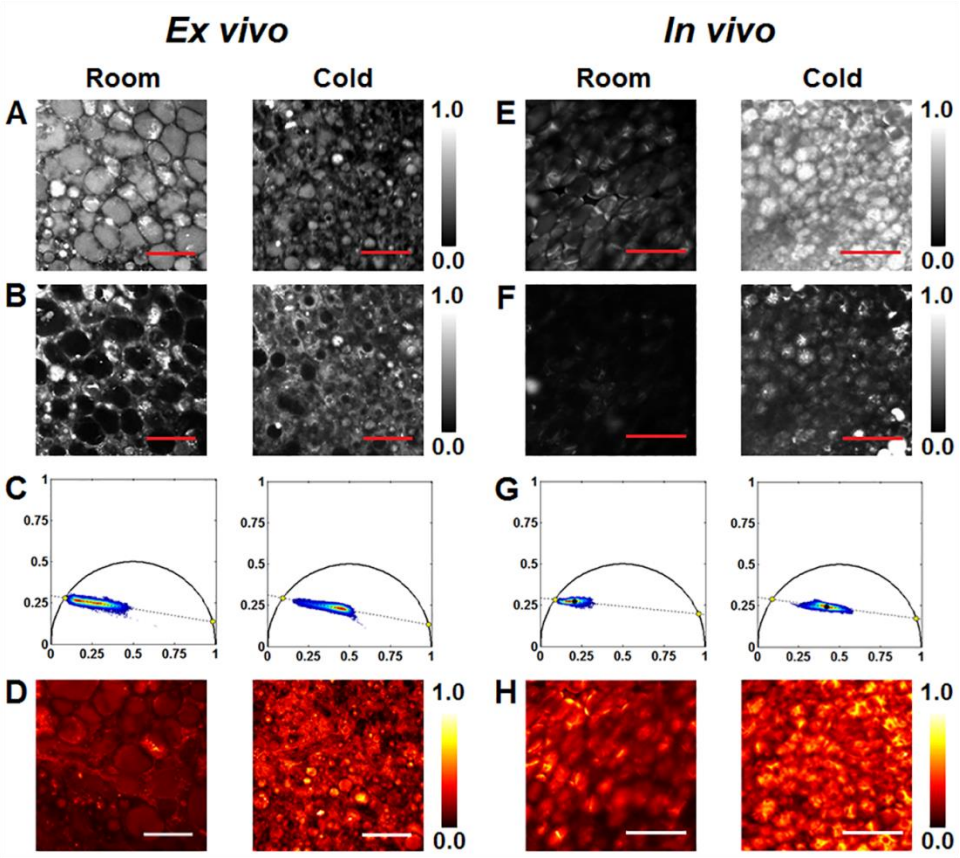

fig. S5. Ex vivo and in vivo raw data set for BAT under the treatment of cold activation, corresponding to representative images shown in Fig. 4. (**A** and **E**) Raw NADH and (**B** and **F**) raw FAD images used to generate redox ratio map. (**C** and **G**) Phasor plots showing the clustering of pixels in the g-s plane. (**D** and **H**) Raw NADH images corresponding to the clone stamped mitochondria images shown in Fig. 4H and N. Scale bar in A, B and D: 50 μm. Scale bar in E, F and H: 100 μm.

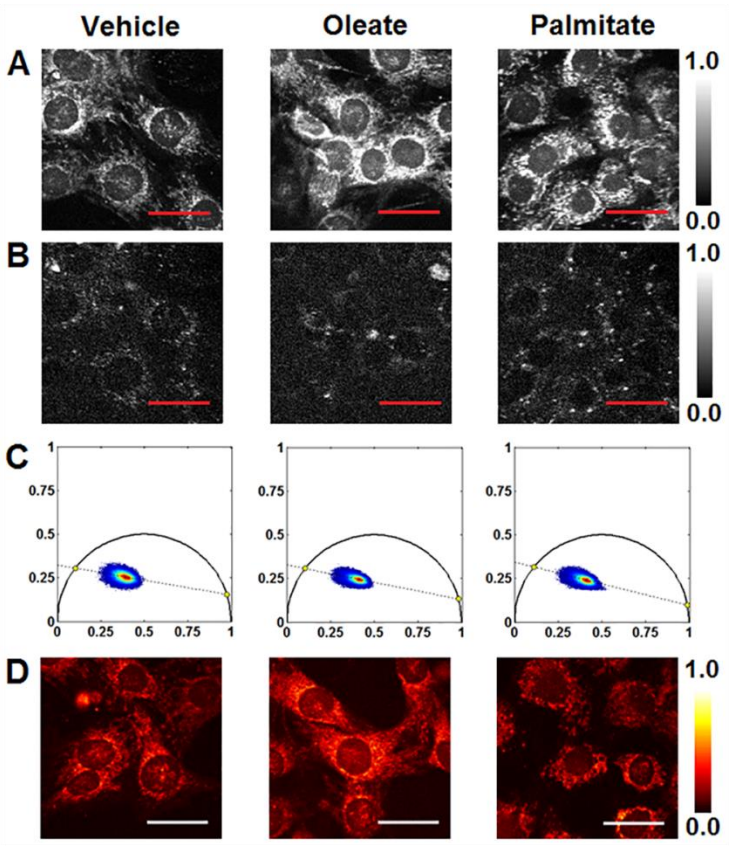

fig. S6. Raw data set for C2C12 cells at various stages of β-oxidation, corresponding to representative images shown in Fig. 5 (A to F). (**A**) Raw NADH and (**B**) raw FAD images used to generate redox ratio map. (**C**) Phasor plots showing the clustering of pixels in the g-s plane. (**D**) Raw NADH images corresponding to the clone stamped mitochondria images shown in Fig. 5E. Scale bar: 30 μm.

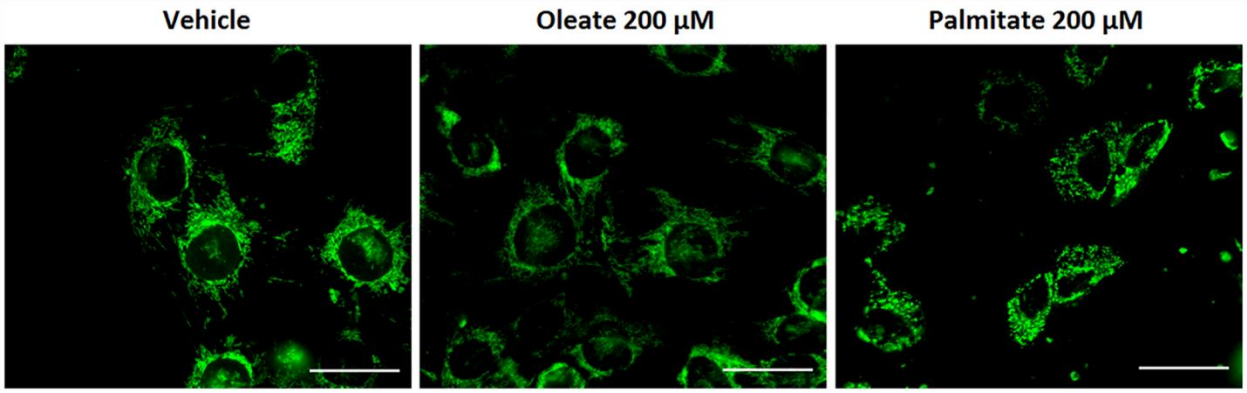

fig. S7. Fluorescence images of C2C12 cells with MitoTracker Green FM staining under different fatty acids supplement. Scale bar: 30 µm.

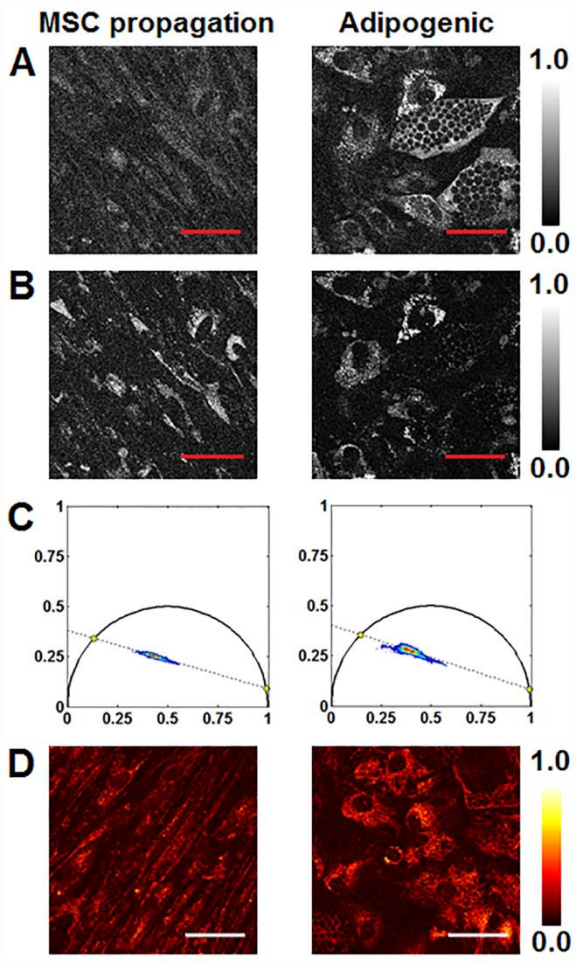

fig. S8. Raw data set for MSCs during lipogenesis, corresponding to representative images shown in Fig. 5 (G to L). (**A**) Raw NADH and (**B**) raw FAD images used to generate redox ratio map. (**C**) Phasor plots showing the clustering of pixels in the g-s plane. (**D**) Raw NADH images corresponding to the clone stamped mitochondria images shown in Fig. 5K. Scale bar: 50 µm.

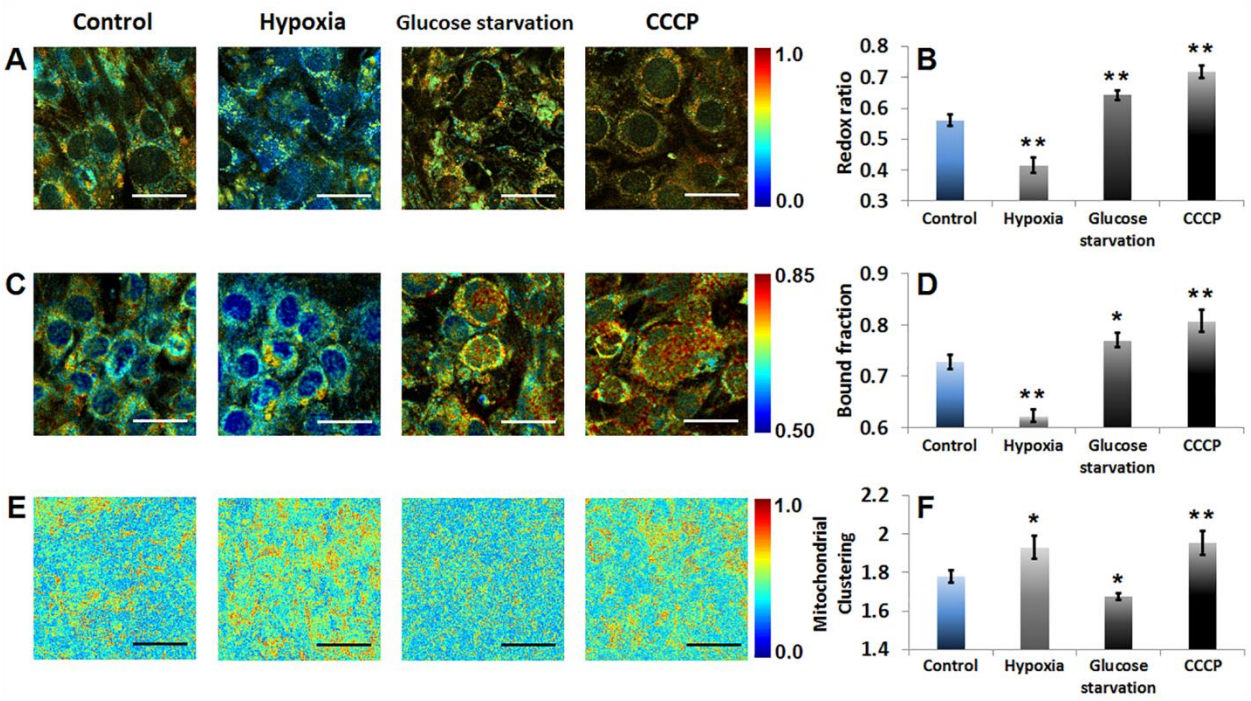

fig. S9. Optical readouts of C2C12 myoblasts in response to hypoxia, glucose starvation, or CCCP-induced chemical uncoupling. (**A**) Representative maps of redox ratio. (**B**) Means and standard deviations of redox ratio. (**C**) Representative maps of bound NADH fraction. (**D**) Means and standard deviations of bound NADH fraction. (**E**) Representative images of clone stamped mitochondria. (**F**) Mean and standard deviation of mitochondrial clustering. For the representative images shown in A, C and E corresponding to hypoxia treatment, data were collected immediately after hypoxia exposure. The significance symbols on top of hypoxia, glucose starvation and CCCP bars reveal significant differences compared with the control group. n = 4 cultures/group. Scale bar: 30 μm. *, $p < 0.05$; **, $p < 0.01$.

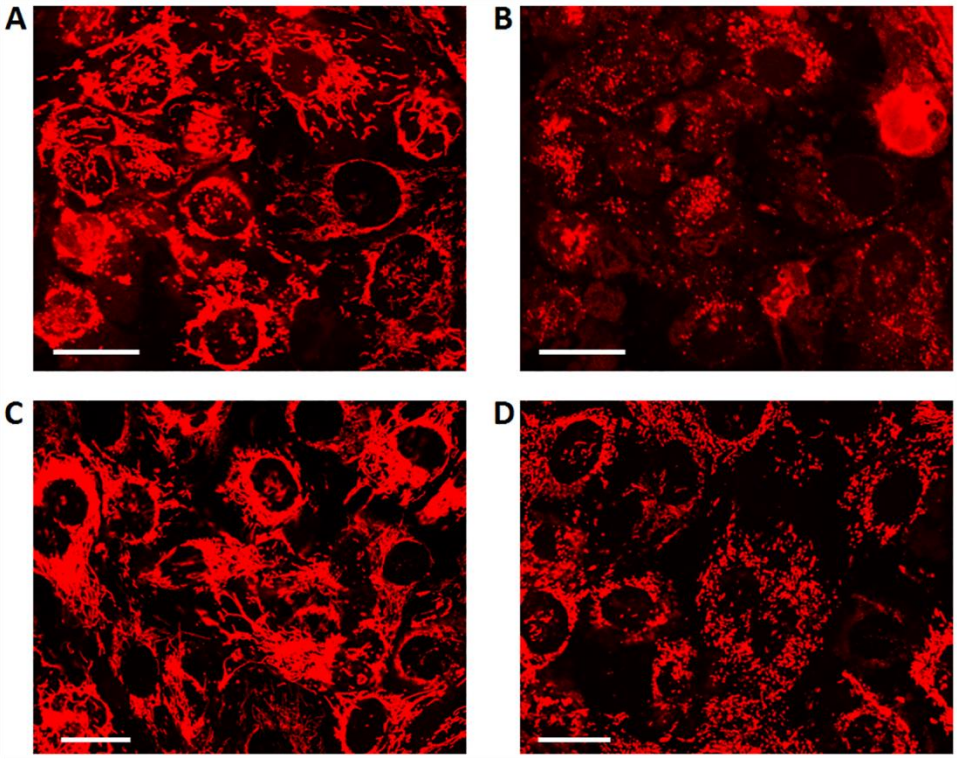

fig. S10. Fluorescence images of C2C12 cells stained with tetramethylrhodamine ethylester (20 nM) under various treatments. (**A**) C2C12 in control media. (**B**) Same image field as (A) immediately after CCCP treatment. (**C**) Glucose Starvation. (**D**) Hypoxic treatment. Scale bar: 20 µm.

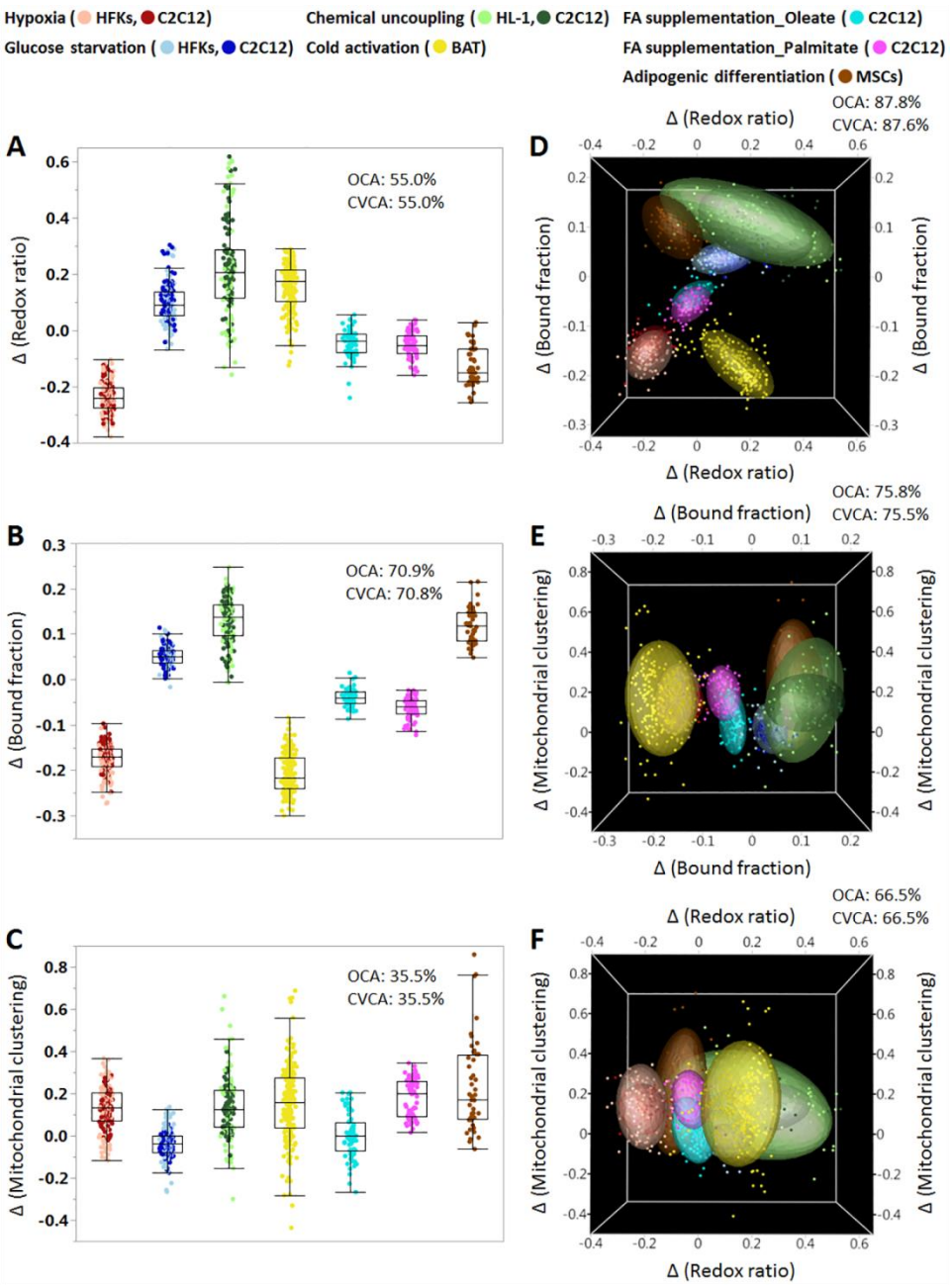

fig. S11. Classification of metabolic pathways using only one or two of the three optical metrics. Utilization of relative changes in (**A**) redox ratio, (**B**) NADH bound fraction, (**C**) mitochondrial clustering, (**D**) both redox ratio and NADH bound fraction, (**E**) both NADH bound fraction and mitochondrial clustering and (**F**) both redox ratio and mitochondrial clustering to distinguish different metabolic perturbations. The classification accuracy values are labeled along with each approach. Colors used for representation of the different perturbations and biological specimens are shown on top. For each of the perturbations where data from multiple cell lines are shown, light and dark hues are utilized to

differentiate between biological specimens. OCA: original classification accuracy; CVCA: cross-validated classification accuracy.

table S1. Individual heterogeneity index for each optical metric under different perturbation.

Pathway	Treatment	Redox ratio	Bound fraction	Mitochondrial clustering
Glycolysis and glutaminolysis	Normal media	0.015±0.002	0.008±0.001	0.081±0.004
	Hypoxia	0.017±0.005	0.014±0.004*	0.189±0.015*
	Glucose starvation	0.025±0.007	0.008±0.001	0.103±0.009
Chemical uncoupling	Control	0.045±0.002	0.008±0.004	0.071±0.020
	CCCP	0.102±0.011*	0.026±0.001*	0.126±0.013*
Cold activation_ *ex vivo*	Room	0.033±0.002	0.029±0.005	0.064±0.025
	Cold	0.030±0.003	0.022±0.005	0.077±0.018
Cold activation_ *in vivo*	Room	0.033±0.003	0.010±0.007	0.220±0.010
	Cold	0.035±0.003	0.017±0.013	0.244±0.027
β-oxidation	Vehicle	0.009±0.001	0.008±0.002	0.055±0.019
	Oleate	0.018±0.002*	0.010±0.002	0.140±0.022*
	Palmitate	0.012±0.001	0.011±0.002	0.138±0.010*
Lipid synthesis	MSC propagation	0.015±0.004	0.015±0.003	0.070±0.006
	Adipogenic	0.037±0.009*	0.021±0.004	0.137±0.030*

The significance symbol indicates significant difference compared with corresponding control in each experiment. Differences are evaluated using an ANOVA with post-hoc Tukey HSD test if there are multiple groups (glycolysis and glutaminolysis, and β-oxidation). Otherwise a two-tailed t-test is used. *, $p < 0.05$.

movie S1. Dynamic redox ratio maps of HFKs treated by normal media. Redox ratio values as indicated by the hues of the redox ratio map remain constant throughout the entire duration of the experiment. Scale bar: 20 μm.

movie S2. Dynamic redox ratio maps of HFKs treated by hypoxia media. The redox ratio map shows lower redox ratio values (blue hues) immediately after the induction of hypoxia. The redox ratio gradually recovers toward baseline levels during the first 30 min. Scale bar: 20 μm.

movie S3. Dynamic redox ratio maps of HFKs treated by no-glucose media. Redox ratio values gradually increase (redder hues) during the first 30 min after the induction of glucose starvation. Scale bar: 20 μm.

List of abbreviations

Acetyl-coA	acetyl coenzyme A
ANOVA	analysis of variance
AST	aspartate transaminase
ATP	adenosine triphosphate
BAT	brown adipose tissue
CCCP	carbonyl cyanide m-chlorophenyl hydrazine
CVCA	cross-validated classification accuracy
DMEM	dulbecco's modified eagle medium
ETC	electron transport chain
ETF	electron transport flavoprotein
FAD	flavin adenine dinucleotide
$FADH_2$	reduced flavin adenine dinucleotide
FBS	fetal bovine serum
FFA	free fatty acid
G3P	glycerol-3-phosphate
HFK	human foreskin keratinocyte
HSD	honest significant difference
IACUC	institutional animal care and use committee
LCFA	long-chain fatty acid
LDH	lactate dehydrogenase
LipDH	lipoamide dehydrogenase
MDH	malate dehydrogenase
MEM	minimum essential medium
MSCs	mesenchymal stem cells

NA	numerical aperture
NAD(P)H	reduced nicotinamide adenine dinucleotide phosphate
NAD^+	nicotinamide adenine dinucleotide
NADH	reduced nicotinamide adenine dinucleotide
NEAA	non-essential amino acids
OCA	original classification accuracy
PDH	pyruvate dehydrogenase
PMT	non-descanned photomultiplier tube
PSD	power spectral density
ROS	reactive oxygen species
SAS	statistical analysis system
SF-DMEM	serum-free dulbecco's modified eagle medium
SPSS	statistical product and service solutions
TCA	tricarboxylic acid
TCSPC	time-correlated single photon counting
TPEF	two-photon excitation fluorescence
UCP1	uncoupling protein 1